

## A Mass-Flux Cumulus Parameterization Scheme across Gray-Zone Resolutions

YOUNG CHEOL KWON AND SONG-YOU HONG

*Korea Institute of Atmospheric Prediction Systems, Seoul, South Korea*

(Manuscript received 24 January 2016, in final form 17 October 2016)

### ABSTRACT

A method that enables a mass-flux cumulus parameterization scheme (CPS) to work seamlessly in various model grids across CPS gray-zone resolutions is proposed. The convective cloud-base mass flux, convective inhibition, and convective detrainment in the simplified Arakawa–Schubert (SAS) scheme are modified to be functions of the convective updraft fraction. The combination of two updraft fractions is used to modulate the cloud-base mass flux; the first one depends on the horizontal grid space and the other is a function of the grid-scale and convective vertical velocity. The convective inhibition and detrainment of hydrometeors are also modified to be a function of the grid-size-dependent convective updraft fraction.


A set of sensitivity experiments with the Weather Research and Forecasting (WRF) Model is conducted for a heavy rainfall case over South Korea. The results show that the revised SAS CPS outperforms the original SAS. At 3 and 1 km, the precipitation core over South Korea is well reproduced by the experiments with the revised SAS scheme. On the contrary, the simulated precipitation is widespread in the case of the original SAS experiment and there are multiple spurious cores when the CPS is removed at those resolutions. The modified mass flux at the cloud base is found to play a major role in organizing the grid-scale precipitation at the convective core. A 1-month simulation at 3 km confirms that the revised scheme produces slightly better summer monsoonal precipitation results as compared to the typical model setup without CPS.

### 1. Introduction

The representation of cumulus convection, generally called cumulus parameterization, has almost always been at the core of efforts to numerically model the atmospheric phenomena because cumulus convection plays a central role in most of the interactions between physical processes in the atmosphere (Arakawa 2004). This is because a cumulus parameterization scheme (CPS) should represent the impacts of convection in terms of environmental conditions, whereas a microphysics scheme (MPS) expresses the precipitation with grid-resolved variables. The MPS is assumed to be relatively robust, since it activates the precipitation processes when the grid-cell mean relative humidity is greater than 100%. It is noted that some MPSs produce condensates in the presence of subsaturation (e.g., Zhao and Carr 1997). The parameterizations of subgrid fluxes in CPSs conceptually

differ from one scheme to another. The complexity of the convective subgrid-scale processes led to a wide variety of CPSs. The main classes are the adjustment type (Betts and Miller 1986), moisture convergence (Kuo 1974), and the mass-flux type (e.g., Arakawa and Schubert 1974; Tiedtke 1989; Kain and Fritsch 1990; Grell 1993).

Continuous efforts to improve the skill of weather forecasts and simulated climatology through revisions of existing CPSs have been made. For instance, Han and Pan (2011) improved the skill of precipitation forecasts in the Global Forecast System (GFS) of the National Centers for Environmental Prediction (NCEP) by revising the cloud microphysics in the simplified Arakawa–Schubert (SAS) scheme that was adapted from Grell (1993). Bechtold et al. (2014) also achieved a significant improvement in the diurnal cycle of precipitation by introducing an equilibrium concept between the parameterized cumulus convection and planetary boundary layer forcing. Qiao and Liang (2014) examined the abilities of 12 different CPS

 Denotes content that is immediately available upon publication as open access.

Corresponding author e-mail: Song-You Hong, songyou.hong@kiaps.org

DOI: 10.1175/MWR-D-16-0034.1

© 2017 American Meteorological Society



This article is licensed under a [Creative Commons Attribution 4.0 license](http://creativecommons.org/licenses/by/4.0/) (<http://creativecommons.org/licenses/by/4.0/>).

schemes in reproducing summer floods and figured out that the incorporation of large-scale instability into the subgrid fluxes is a promising way to improve the summer rainfall climatology over the Great Plains of the United States. Wang et al. (2015) investigated the impacts of the triggering function of two CPSs, the SAS and Zhang and McFarlane (1995) schemes in a GCM, and showed that the convective inhibition and level of launching parcel are crucial to the successful prediction of diurnal rainfall cycles over the Great Plains.

It is noted that all of the aforementioned studies utilize horizontal grid spacing greater than 10 km, in which the portion of updraft clouds may be negligible relative to that of the model grid box. This assumption is considered valid in climate communities, because the horizontal grid spacing of GCMs is on the order of 100 km. This assumption is still valid in the NWP community for medium-range forecasts that use global models. Assuming that the scale of the parameterized convective updrafts ranges around  $10 \text{ km}^2$ , the horizontal resolution of global NWP models (e.g., 10 km in the ECMWF model) still satisfies the assumption, but the assumption certainly breaks down when the grid is smaller than 5 km. Therefore, regional models having grid sizes smaller than 5 km exclude CPSs, which is assumed to be a cloud-resolving scale. At that resolution, numerous studies have been conducted to improve the predictability of simulated results by investigating the sensitivity of the simulation results to MPSs (e.g., Bryan and Morrison 2012; Schwartz and Liu 2014; McMillen and Steenburgh 2015). However, there is no specific MPS that outperforms the others (Clark et al. 2012).

A plausible reason for this lies in the fact that CPSs are removed, although the precipitating convection is not fully resolved by grid-scale forcing at that resolution. This issue, the so-called gray zone, has been raised in the modeling community (Hong and Dudhia 2012). Problems appear in physics as NWP models go to finer scales where there are gray zones in which the explicit model dynamics are partly capable of resolving features that are parameterized at coarser scales. Since Gerard et al. (2009) demonstrated the success of a CPS at 3–8 km by allowing subgrid prognostic updraft effects that closely interact with the microphysics, there have been significant efforts to represent the CPSs at 1–10-km grid spacing (Gomes and Chou 2010; Arakawa et al. 2011; Arakawa and Wu 2013; Grell and Freitas 2014). Gomes and Chou (2010) introduced the scale dependence of convective and grid-scale precipitation by adding a resolution-dependent parameter in the Kain–Fritsch CPS (Kain 2004). Grell and Freitas (2014; hereafter the GF scheme) also introduced a grid-size dependency of the mass flux following the ideas proposed in

Arakawa et al. (2011). In the GF scheme, the subgrid-scale vertical eddy flux is gradually suppressed as the grid spacing is decreased. Fowler et al. (2016) implemented the GF scheme into a global model with variable meshes from 3 to 50 km, and demonstrated that over the refined region of the mesh, the GF scheme performs as a precipitating shallow convective scheme, whereas over the coarse region of the mesh, GF acts as a conventional CPS. Zheng et al. (2016) introduced the grid-size dependency in the in-cloud properties, such as the grid-scale vertical velocity and convective entrainment in the Kain–Fritsch scheme, and demonstrated the improvement of the location and intensity of precipitation in high-resolution (3 and 9 km) forecasts. Meanwhile, Kuell et al. (2007) introduced a hybrid approach wherein only updraft and downdraft are parameterized with a net mass transport. The environmental subsidence is treated by the grid-scale equations by splitting the total mass flux in the continuity equation into a grid-scale and a subgrid-scale contribution. All these studies are efforts to represent a smooth transition from CPS-induced to MPS-induced precipitation at gray-zone scales.

The purpose of this study is to introduce a scale-dependent SAS CPS across gray-zone resolutions. This study is an extension of Lim et al. (2014), who introduced a grid-spacing dependency in the convective trigger function of the SAS CPS. Here, convective inhibition, mass flux, and detrainment of hydrometeors are modified with a function of the horizontal grid spacing. These modifications are tested in the WRF Model for a heavy rainfall event over South Korea, focusing on the 3- and 1-km results. In section 2, the changes in the SAS scheme are described with respect to the experimental design. Results are analyzed in section 3, and our conclusions are given in the final section.

## 2. Method

### *a. A brief overview of the SAS scheme*

The SAS CPS has been used in the operational NCEP GFS system, and its performance and reliability are well documented. There are many papers in the literature discussing the features and details of GFS SAS (e.g., Grell 1993; Pan and Wu 1995; Hong and Pan 1998; Han and Pan 2011; Lim et al. 2014). Thus, only the part of the GFS SAS scheme related to our study will be summarized in the following.

In the SAS scheme, a convective inhibition (CIN) factor is used in order to modulate the trigger of convection. The CIN in the GFS SAS scheme is defined as the pressure difference between the parcel starting level and the level of free convection (LFC). This difference indicates an obstacle for a potential convective parcel to overcome the negative buoyancy necessary to initiate

convective activity. When this pressure difference is larger than a critical value, which varies within the range of 120–180 hPa in proportion to the grid-scale vertical velocity, the SAS scheme assumes that the parcel will not reach the LFC. Therefore, in this case, subgrid-scale convection will not be triggered.

The cloud-base mass flux is one of the important quantities that determine the strength of subgrid-scale convection. Currently, the cloud-base mass flux in SAS is defined as

$$m_b = \frac{A - f_1 A_c}{\tau_{\text{cnv}}} \frac{m'_b \Delta t'}{A - A'}, \quad (1)$$

where  $A$  and  $A_c$  are the cloud work function at a grid point and the critical cloud work function calculated from the observations, respectively. Here,  $f_1$  is a coefficient varying with the large-scale vertical velocity (Lim et al. 2014), and  $A'$  is the modified cloud work function obtained from thermodynamic variables with an arbitrary amount of mass flux  $m'_b \Delta t'$ , while  $\tau_{\text{cnv}}$  is the convective adjustment time scale, which varies between 1200 and 3600 s depending on the model time step and grid-scale updraft velocity.

Inside the convective updraft, the excessive moisture of the SAS scheme is converted to precipitation (auto-conversion), detrained to grid-scale cloud condensate, or carried with the updraft. The amounts converted to precipitation and detrainment are determined by the parameters  $C_0$  and  $C_1$  (Han and Pan 2011), respectively, with the current setting of  $C_0 = C_1 = 0.02 \text{ m}^{-1}$ . The detrainment of convective cloud water is only allowed above the level of the minimum moist static energy of the convective column.

#### *b. Definition of the convective updraft fraction $\sigma$ and modifications for gray-zone SAS*

The proper definition of the convective updraft fraction  $\sigma$  is one of the most crucial aspects for the successful development of a scale-aware CPS across the gray zone. The convective updraft fraction  $\sigma$  is the areal ratio of the convective updraft  $A_c$  over the grid box  $A_g$ , so the magnitude of  $\sigma$  varies from 0 to 1. If  $\sigma = 0$ , then the whole grid box is free of convection, whereas  $\sigma = 1$  means the whole grid box is completely covered by the convective updraft.

Two different quantities are introduced to define  $\sigma$  in this study. Note that the updraft fraction introduced in our study is a rather pragmatic approach in order to modify the high-resolution behavior of the SAS CPS. The first quantity assumes that  $\sigma$  is only a function of grid size  $\Delta x$ , with the assumption that the convective cloud updraft fraction is the averaged invariant convection size,

about 1.5–2 km in radius. The functional form in Hong and Pan (1998) with a slight modification is used for defining this grid size-dependent  $\sigma_1$ :

$$\sigma_1 = 1 - \frac{1}{\pi} \left\{ \sigma_{\text{con}} \left[ (\Delta x - \Delta 1) + \frac{\pi}{2} \right] \right\} \quad \text{and} \quad (2)$$

$$\sigma_{\text{con}} = \frac{\tan(0.4\pi)}{\Delta 1 - \Delta 2},$$

where  $\Delta x$  is the horizontal grid size (m) of a model,  $\Delta 1$  and  $\Delta 2$  are the values for determining the shape of the curve and are set to 5000 and 1000 m, respectively. The distributions of  $\sigma_1$  with respect to the horizontal grid size  $\Delta x$  are shown in Fig. 1. The fraction of the convection-free area represented by  $(1 - \sigma_1)$  is also denoted with a dotted line in Fig. 1. Equation (2) is slightly modified to make  $\sigma_1$  become 1.0 at  $\Delta x = 100$  m resolution in order to consider the fact that the convection can be explicitly resolved below that resolution.

The other updraft fraction  $\sigma_2$  assumes that the area of the convective updraft is allowed to vary with the thermodynamical and dynamical conditions of the atmosphere. This second method therefore accommodates the variations of  $\sigma$  due to the grid-scale vertical velocity and the convective updraft velocity inside a cloud. The underlying idea of the method is that the strength of the gridpoint updraft will gradually approach to that of the convective updraft when the convective area in the grid box becomes dominant (Pan et al. 2014). The gridbox updraft velocity-dependent  $\sigma$  ( $\sigma_2$ ) is defined as

$$\sigma_2 = \frac{\bar{w}}{\bar{w}_c}, \quad (3)$$

where  $\bar{w}$  is the vertical velocity at a grid point that is vertically averaged between cloud bottom and top and  $\bar{w}_c$  represents the averaged convective updraft velocity. Note that  $\bar{w}$  is originally formulated as the maximum vertical velocity in a grid column. Based on Eq. (3), the grid box will be fully covered by convection ( $\sigma_2 = 1$ ) when the magnitude of the gridpoint updraft becomes the same as that of the convective updraft. If the gridpoint upward velocity is much smaller than the convective updraft, this method assumes that the convective updraft fraction is very small. See Pan et al. (2014) for a detailed description of Eq. (3).

The two methods of defining  $\sigma$  used in this study each have their own strong and weak points. The first method assumes that the convective area is the same everywhere and disregards the possibility that convection can occupy several grid boxes, as shown in Fig. 8 of Arakawa et al. (2011). This definition of  $\sigma_1$  does not reflect the cloud properties but produces a wide range of variations of convective updraft fraction with respect to grid size.

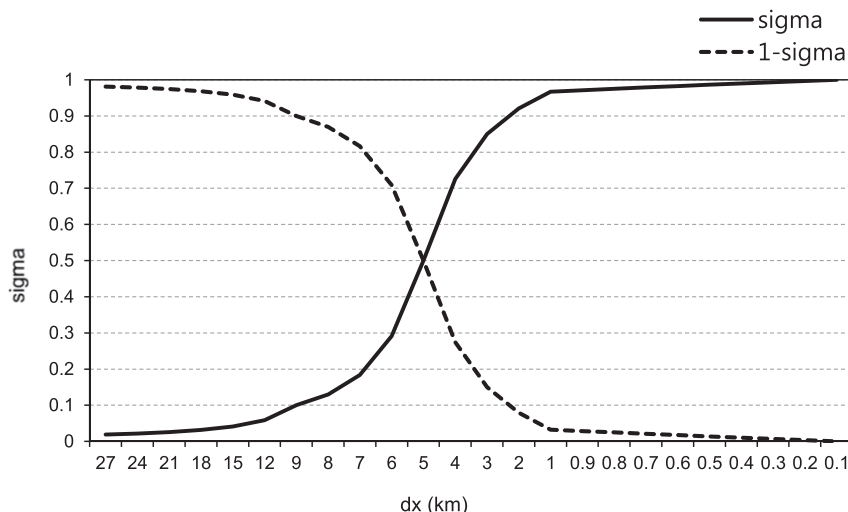


FIG. 1. Convective updraft fraction  $\sigma_1$  with respect to the horizontal grid resolution (km). When  $\sigma_1$  reaches one, the whole grid box is covered by convection.

On the other hand, the second method reflects the strength of the grid-scale vertical motion that would activate more grid-resolvable precipitation through MPS processes at higher resolutions. The grid-scale updraft velocity  $\bar{w}$  is stronger at higher resolutions, whereas the convective updraft  $\bar{w}_c$  is nearly independent of grid size  $\Delta x$ . Preliminary analyses revealed that  $\bar{w}$  rarely reaches the magnitude of  $\bar{w}_c$ . For example,  $\sigma_2$  barely reaches 0.3 even at  $\Delta x = 1$  km.

Three modifications are made to the SAS CPS to introduce scale-aware capability: 1) cloud-base mass flux, 2) CIN, and 3) convective cloud water detrainment (DTR). While  $\sigma_1$  is applied to all three modifications,  $\sigma_2$  is only applied to the cloud-base mass modification as in the following equations:

$$m_b = (1 - \sigma_1)(1 - \sigma_2)m_b^{\text{org}}, \quad (4)$$

$$\text{CIN}_{\text{th}} = (1 - \sigma_1)\text{CIN}_{\text{th}}^{\text{org}}, \quad \text{and} \quad (5)$$

$$\text{DTR} = \sigma_1 \text{DTR}^{\text{org}}. \quad (6)$$

The superscript *org* represents the original value calculated from the SAS CPS before applying scale-aware factor  $\sigma$ . As the grid size becomes finer, the role of the CPS should gradually decrease as the grid-scale saturation becomes active. A threshold value of CIN is denoted  $\text{CIN}_{\text{th}}$ . If the pressure difference between the level of the updraft-originating parcel and the level of free convection (LFC) is larger than  $\text{CIN}_{\text{th}}$ , then convection will not be triggered. The smaller  $\text{CIN}_{\text{th}}$  would act to suppress the triggering of convection and vice versa. Therefore, convective inhibition should be larger, and the cloud-base mass flux becomes smaller at finer resolutions (bigger  $\sigma_1$ ), as in Eqs. (4) and (5). In the original

SAS, the hydrometeors detrained from the CPS are added to the grid-resolvable hydrometeors in MPS processes, irrespective of horizontal resolution. We presume that the amount of detrained hydrometeors from CPS can be added to the grid-resolvable water substance when the convective area is comparable to grid size. In other words, the addition of hydrometeors to the MPS prognostic variable should become smaller at lower resolutions since it spreads over the whole grid box, and then that amount is available to grid-scale processes [Eq. (6)].

Regarding cloud-base mass flux,  $(1 - \sigma)^2$  should be the factor to make it scale aware, as in the derivation of Arakawa and Wu (2013), also adapted in Grell and Freitas (2014). The mixture of  $\sigma_1$  and  $\sigma_2$  for the quadratic form of the modification factor to cloud-base mass flux is adopted in this study, as in Eq. (4). The rationale of using both  $\sigma_1$  and  $\sigma_2$  is that they seem to complement each other's weaknesses. The use of  $(1 - \sigma_1)^2$  lacks a physical base but produces enough resolution dependency. On the contrary,  $(1 - \sigma_2)^2$  has a physical background, but it does not show enough variation of the convective updraft fraction in the gray-zone resolutions.

### c. Experimental design

A flash-flooding heavy rainfall event that occurred from 27 to 29 July 2011 over the central part of South Korea (Fig. 2) is selected as a convection case to investigate the impacts of the modifications in SAS CPS on the reproduction of a rainfall core. The daily precipitation on 27 July 2011, 301.5 mm, set a record for maximum rainfall over Seoul in July, and most of

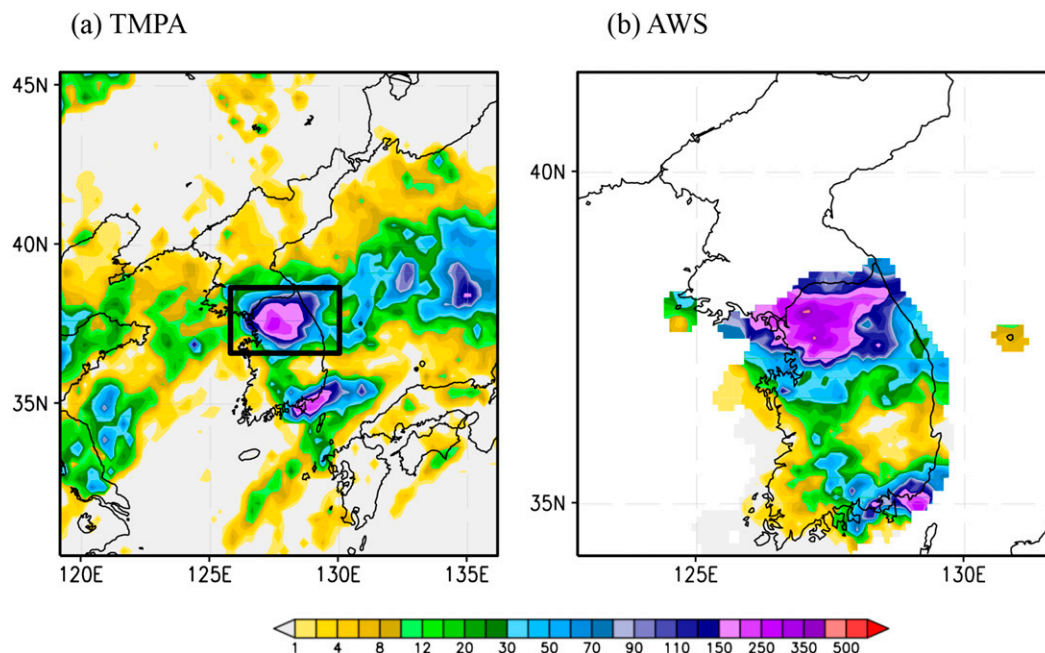


FIG. 2. The 24-h accumulated precipitation ( $\text{mm day}^{-1}$ ) at 1200 UTC 27 Jul 2011 obtained from (a) the Tropical Rainfall Measuring Mission (TRMM) Multisatellite Precipitation Analysis (TMPA) and (b) the automatic weather station (AWS) observations. The inner rectangle in (a) designates the area for the average in Fig. 7.

the rainfall was observed from 1200 UTC 26 July to 1200 UTC 27 July 2011. Thus, this 24-h accumulated precipitation was evaluated in this study. This intense convection is induced by a supply of abundant warm and humid air directed toward the midwestern region of the Korean Peninsula after being transported from the Yellow Sea. This pattern persisted within a quasi-stationary synoptic environment: the western Pacific subtropical high over the southeast to South Korea and Japan, and a cutoff blocking high over 500 hPa (Jang and Hong 2014). It is easy to analyze the sensitivity of precipitation to the applied CPS because the measurements show a spatial distribution with a single maximum core located near Seoul.

A series of simulations is performed in order to investigate the impacts of scale-aware capability made to SAS CPS. The NCEP SAS in the Advanced Research version of the WRF Model (WRF-ARW; Skamarock et al. 2008) is modified as described in section 2b for the tests. The four nested domains are designed with horizontal resolutions of 27, 9, 3, and 1 km in order to include CPS gray-zone resolutions (Fig. 3). The numbers of horizontal grid points of the four domains are  $178 \times 150$ ,  $259 \times 223$ ,  $355 \times 352$ , and  $403 \times 403$  with the projection center point located at  $38^\circ\text{N}$ ,  $125^\circ\text{E}$ . All experiments consist of one-way nested domains with a Lambert conformal map projection. The number of model level is 51, with a top at 50 hPa.

The physics used in this study are the Noah land surface and soil physics scheme (Chen and Dudhia 2001; Ek et al. 2003), the Yonsei University (YSU) planetary boundary layer (PBL) vertical diffusion scheme (Hong et al. 2006), the Global/Regional Integrated Model system (GRIMs) shallow convection scheme (Hong et al. 2013), the WRF single-moment 5-class (WSM5)

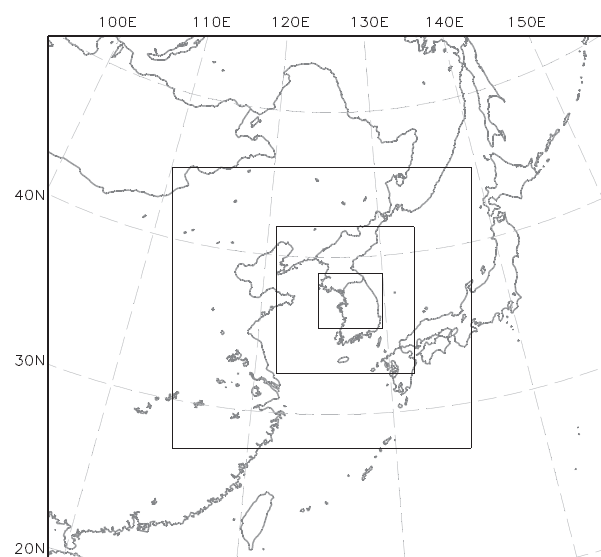


FIG. 3. Model domains of the experiments at 27-, 9-, 3-, and 1-km resolutions.



TABLE 1. List of experiments conducted in this study.

Expt	Description
OSAS	Original NCEP GFS SAS at 27, 9, 3, and 1 km; all with CPS
GSAS	Modified SAS for scale-awareness CIN, mass flux, and detrainment
GCIN	Only active scale-awareness CIN
GCMF	Only active scale-awareness mass flux
GDTR	Only active scale-awareness detrainment
NOCP	As in OSAS, but no CPS at 3 and 1 km

MPS (Hong et al. 2004), and the RRTM with GCM applications radiation scheme (RRTMG) for both incoming shortwave (Iacono et al. 2008) and outgoing longwave (Mlawer et al. 1997) radiation.

Table 1 summarizes the experiments conducted in this study. The gray-zone SAS denoted by GSAS is the experiment with which all three modifications in the previous section are included. Three additional experiments are carried out in order to identify the contributions of each modification. The modifications made only to CIN, cloud-base mass flux, and cloud water detrainment are named GCIN, GCMF, and GDTR, respectively. To avoid the issue of a conventional CPS in gray-zone resolution, numerical simulations with horizontal resolutions finer than 5 km are usually carried out without calling CPSs. The experiments without calling the CPS, denoted by NOCP, are carried at 3 and 1 km. All experiments are performed for 48 h, from 0000 UTC 26 July to 0000 UTC 28 July 2011. The initial conditions of the experiment utilize the NCEP Final (FNL) analysis data on  $1^\circ \times 1^\circ$  global grids, without specific assimilation of observational data. The nudging frequency along the lateral boundaries used in this study is 6 h and the large-scale flows of the 27-km domains are forced by NCEP FNL data. The following nested domains are conditioned by immediate coarse-resolution domains. An additional test bed for the whole month of July 2011 is designed to statistically evaluate the performance of the revised scheme against the simulation without CPS on a 3-km grid, which is a conventional model setup for grid sizes of less than 5 km.

### 3. Results

The results from the 3-km simulations are focused on in this section by investigating the individual effects of modifications in the SAS CPS, because this is the resolution for most regional models with the CPSs removed (Clark et al. 2012). Since the asymptotic grid size for fully resolving convection is defined at  $dx = 100$  m as in Fig. 1, the 1-km results are also shown. The overall performance of the results for the 27- and 9-km

TABLE 2. Comparison of RMSE and PC with AWS observations, local maximum, simulated precipitation over the location of observed rain core (Precip<sub>core</sub>), and areal average (Avg<sub>dom</sub>) over  $34.2^\circ$ – $41.5^\circ$ N,  $122.8^\circ$ – $131.7^\circ$ E for 24-h accumulated precipitation ( $\text{mm day}^{-1}$ ) at 1200 UTC 27 Jul 2011 across four domains. The value of Avg<sub>dom</sub> for the AWS observations is averaged over domain 4. Best scores for each domain are highlighted in boldface. See Koo et al. (2009) for the details on computing the coefficients.

Domain	Expt	RMSE	PC	Max	Precip <sub>core</sub>	Avg <sub>dom</sub>
1 (27 km)	OSAS	76.67	0.18	117.08	43.43	13.91
	GSAS	<b>68.17</b>	<b>0.56</b>	<b>136.15</b>	<b>59.62</b>	14.05
2 (9 km)	OSAS	80.15	0.004	135.74	29.87	14.53
	GSAS	<b>75.31</b>	<b>0.24</b>	196.95	<b>47.66</b>	<b>15.87</b>
3 (3 km)	OSAS	<b>78.43</b>	0.07	190.57	38.01	17.21
	GSAS	80.29	0.23	<b>477.18</b>	62.44	16.14
	NOCP	81.46	<b>0.31</b>	665.38	<b>92.90</b>	<b>28.68</b>
4 (1 km)	OSAS	92.38	0.17	788.79	54.20	36.32
	GSAS	<b>82.37</b>	<b>0.60</b>	<b>765.28</b>	<b>138.06</b>	<b>41.98</b>
	NOCP	102.33	0.15	2168.55	77.61	63.61
	AWS			442.28	186.63	47.39

simulations is briefly described in terms of the effects of modifications in Eqs. (4)–(6).

#### a. Overall performance

The various measures of the modeled precipitation are compared in Table 2. Scores for the simulated precipitation over the in situ observations [taken from automatic weather stations (AWSs)] over South Korea are computed. The number of automatic weather stations is over 600, and they are approximately 20 km apart. The simulated precipitation data are bilinearly interpolated to the AWS station points in order to calculate the verification scores. The RMSE and pattern correlation (PC) coefficients demonstrate that the precipitation prediction skills of the GSAS run are better when compared to those of the OSAS runs. In particular, the improvement in the 1-km results is obtained for all categories of skill scores. The simulated precipitation is closer to the observed even in the case of the 27-km resolution, which is beyond the gray-zone resolutions. Further testing and analysis suggests that the improvement in 27-km resolution is mostly caused by the modifications in cloud water detrainment. The suppressed detrainment of convective cloud water to the grid-resolvable precipitation physics plays a role in increasing the CPS precipitation and decreasing the MPS precipitation, which results in an organized precipitation band. Improvement in the experiments at a cutting-edge resolution of 9 km is not negligible either. The results from the sensitivity tests when not calling CPS at 3 km confirm the result that NOCP produces a better pattern correlation but with an excessive amount of maximum rainfall. This problematic rainfall peak in

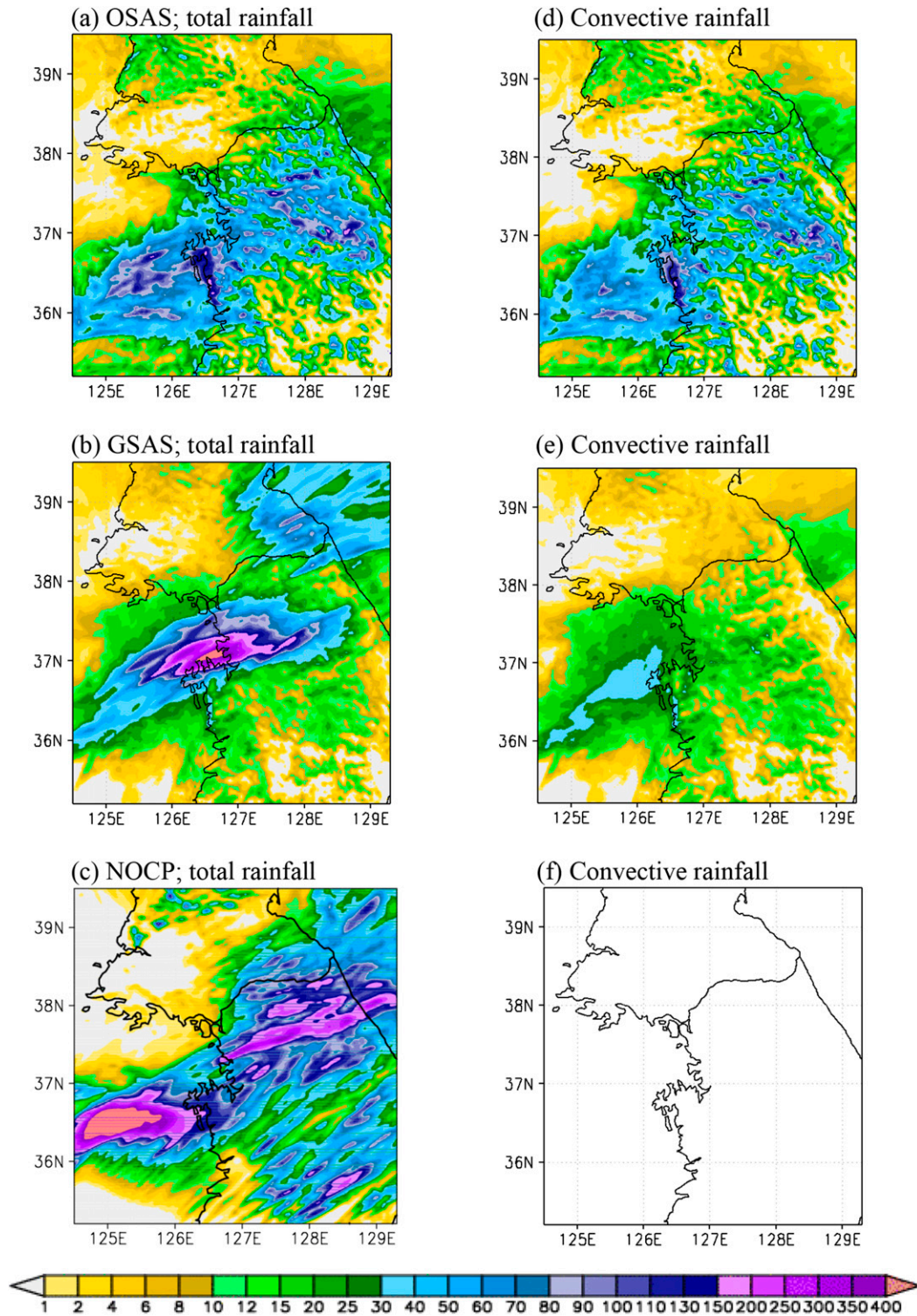


FIG. 4. Spatial distributions of the 24-h accumulated rainfall amount at 1200 UTC 27 Jul 2011 for the 3-km resolution. The results of the (a),(d) OSAS; (b),(e) GSAS; and (c),(f) NOCP are shown; where (left) is total rainfall and (right) is convective precipitation.



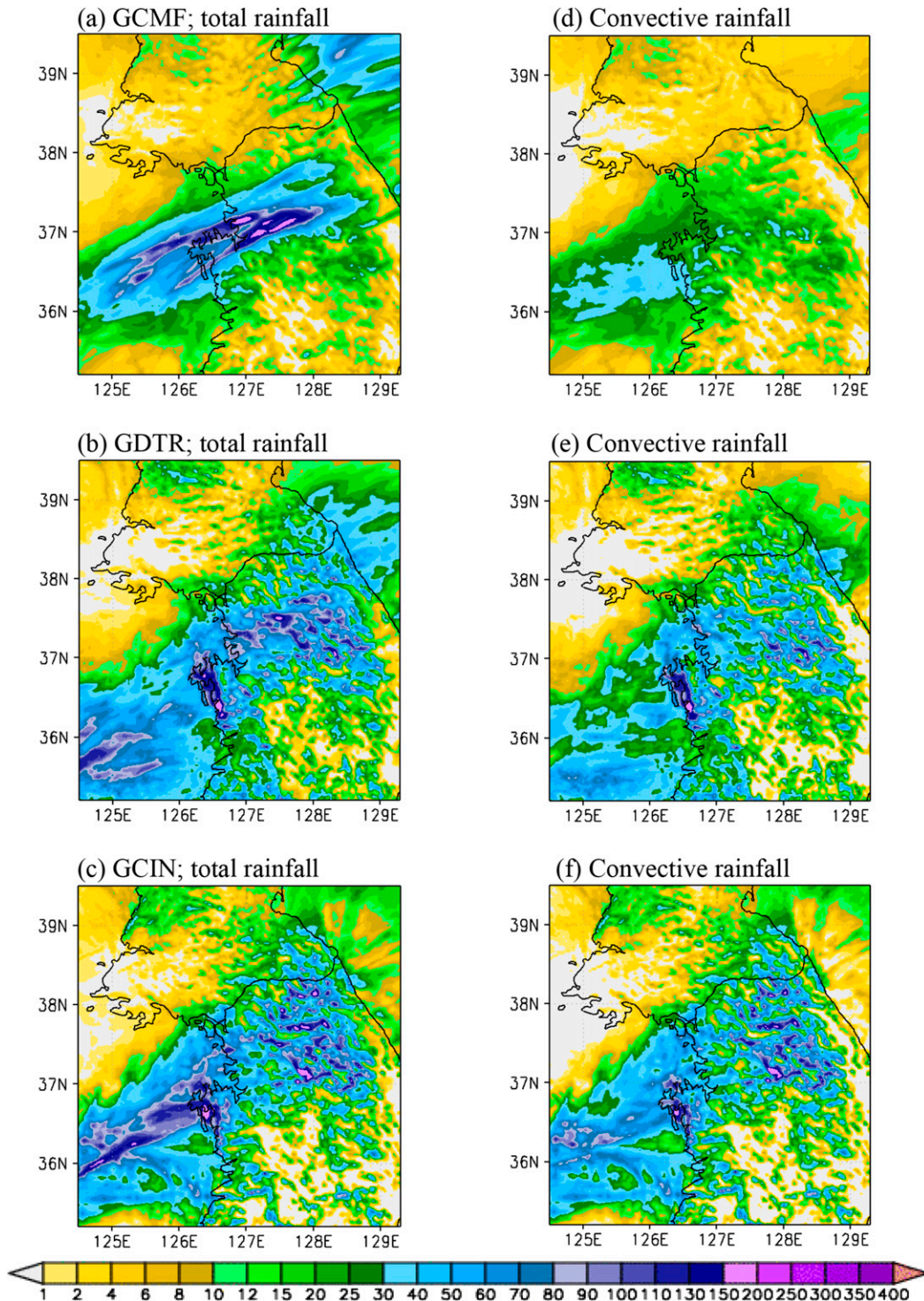


FIG. 5. Spatial distributions of 24-h accumulated rainfall amount at 1200 UTC 27 Jul 2011 for the 3-km resolution. The results of the (a),(d) GCMF; (b),(e) GDTR; and (c),(f) GCIN experiments are shown.

the amount of more than 2000 mm is pronounced at 1 km.

The 24-h accumulated rainfall results simulated by 3-km resolution from 1200 UTC 26 July to 1200 UTC 27 July

2011 are compared in Fig. 4. The precipitation patterns simulated by the OSAS (Fig. 4a) show widespread features instead of a single core in the observed rainfall. The maximum rainfall core of the OSAS is located in the



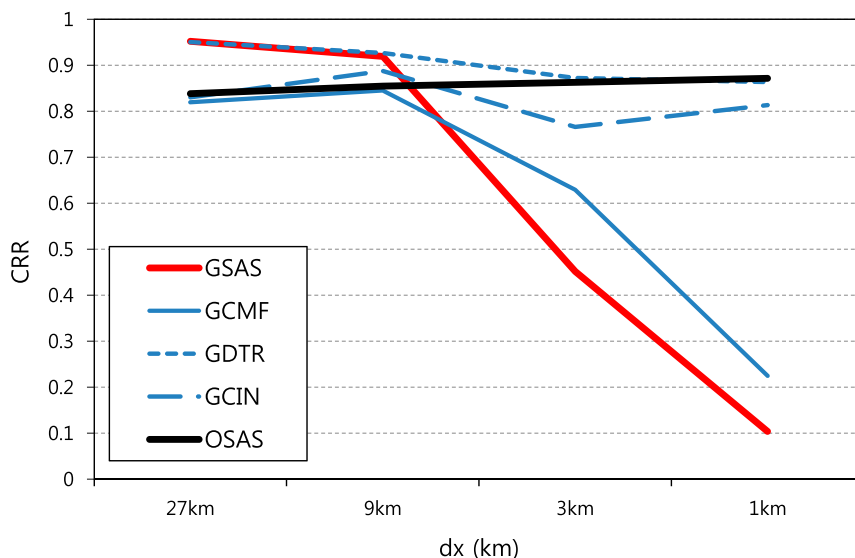


FIG. 6. Convective rain ratio of experimental results for all four domains. The thick red (GSAS) and black (OSAS) lines are the revised SAS and original SAS simulations, respectively. The thin blue (GCMF), thin blue dashed (GCIN), and thin blue dotted (GDTR) lines are for the cloud-base mass flux, trigger, and convective liquid water detrainment simulations, respectively.

coastal region to the southwest of the observed location. While the observed maximum rainfall amount is about 442.3 mm during the period, the OSAS simulation results in only 190.6 mm, less than half of the observed amount. The overall pattern of the GSAS run (Fig. 4b) is improved with a single precipitation core, as seen in the observations. Although the rainfall core is slightly shifted to the west, its magnitude of 477.2 mm is close to the observed value. The simulation without CPS (NOCP; Fig. 4c) produces more organized rainfall patterns than does the OSAS, but it suffers from the problems associated with producing an excessive precipitation core in the southwest region. Although the tabulated scores in Table 2 are comparable for both the GSAS and NOCP runs in terms of root-mean-square error (RMSE) and pattern correlation (PC), the locations of the cores are far away from the observed (shown in Fig. 2a) with a spurious maximum precipitation amount over the ocean of 665.4 mm. A band-type area of precipitation across the central peninsula is also unrealistic. The comparison of the CPS rain reveals that rainfall mostly is produced by the CPS process even over heavy precipitation areas when the OSAS is employed (Fig. 4d). On the other hand, the CPS processes are significantly reduced in the GSAS run (Fig. 4e), which leads to the simulated precipitation core that is mostly due to the MPS scheme.

#### b. Sensitivity experiments

The 3-km-resolution simulated precipitation from the three modifications in the GSAS CPS over the OSAS

CPS (i.e., GCMF, GDTR, and GCIN) is depicted in Fig. 5. It is clear that the overall distribution of the simulated precipitation is largely influenced by the change in the cloud-base mass flux (Figs. 4b and 5a). The location of the rainfall core is similar, but it shows less organized patterns than those from the GSAS run. The amounts of CPS rain are comparable to each other (Figs. 4e and 5d). It is noticeable that the distribution of rainfall in Figs. 5b and 5c more or less follows that in Fig. 4a (OSAS). In terms of the CPS rain, its amount stays relatively similar compared to the modified trigger and detrainment of hydrometeors (cf. Figs. 4d and 5e,f). The smaller effect of the detrainment is due to the fact that the entire portion of the hydrometeors is detrained in the original SAS irrespective of the resolution, whereas the detrained amount of the GSAS is gradually increased to the OSAS value with the grid spacing. Thus, the detrainment effect is more significant at lower resolutions as compared to the original SAS CPS. The overall results from the sensitivity experiments indicate that the impact due to revised detrainment and CIN is not significant, while modification of the cloud-base mass flux is largely responsible for the improvement in the simulated precipitation in the case of the 3-km runs.

The portions of precipitation caused by CPS out of the total rainfall amount [convective rain ratio (CRR)] are analyzed to examine the convective rain contribution at various resolutions (Fig. 6). The CRR of OSAS does not vary enough with respect to grid resolutions, and its CRR ranges from about 0.8 to 0.9 even with a slightly

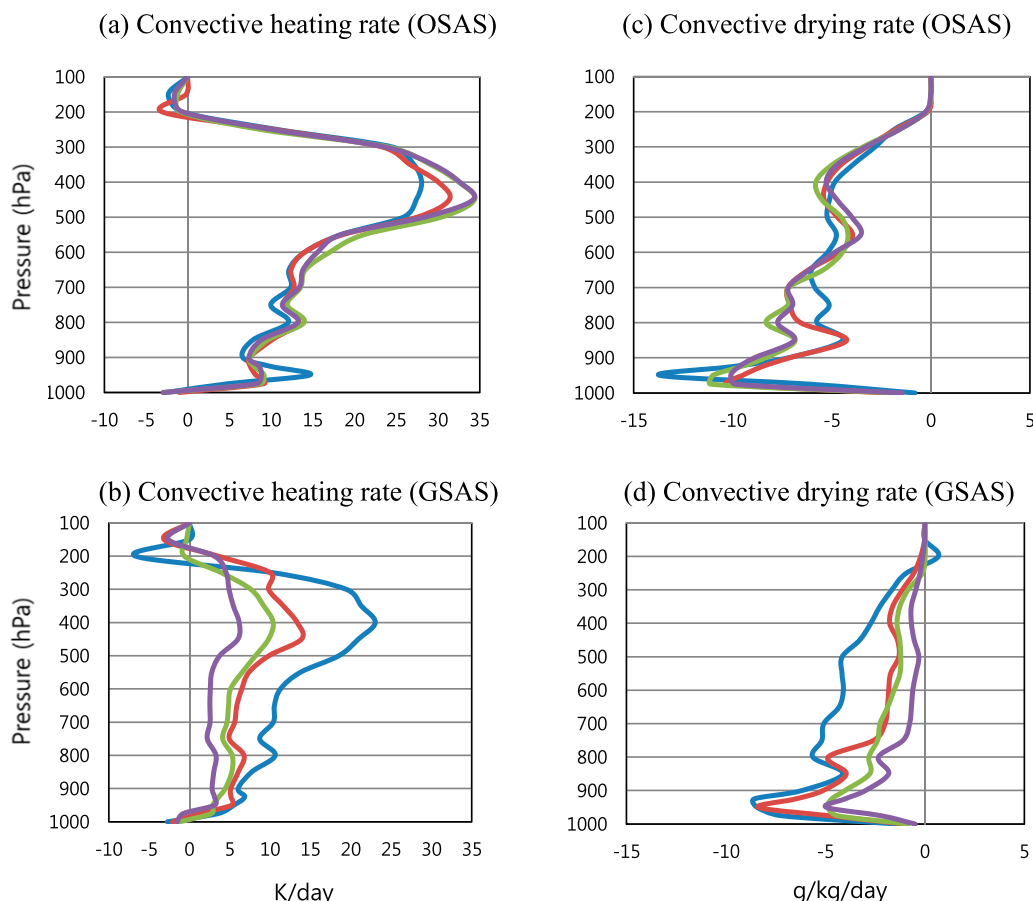
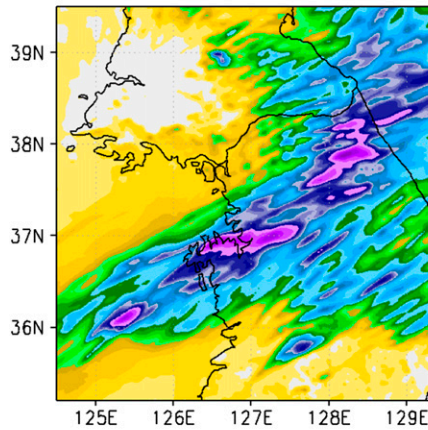


FIG. 7. Vertical profiles of the (left) convective heating and (right) drying rate from the (a),(c) OSAS and (b),(d) GSAS experiments at various horizontal resolutions. Blue, red, green, and purple lines represent  $\Delta x = 27, 9, 3$ , and 1 km, respectively. The box shown in Fig. 2a is the domain for the averaging of the heating and drying rate.

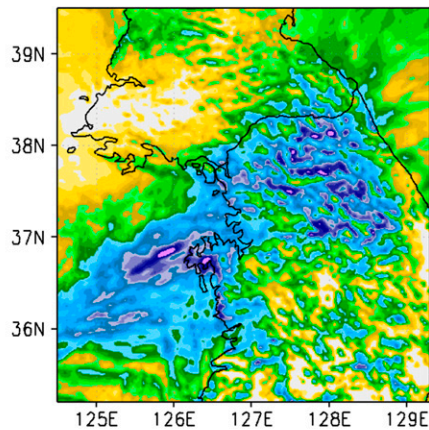
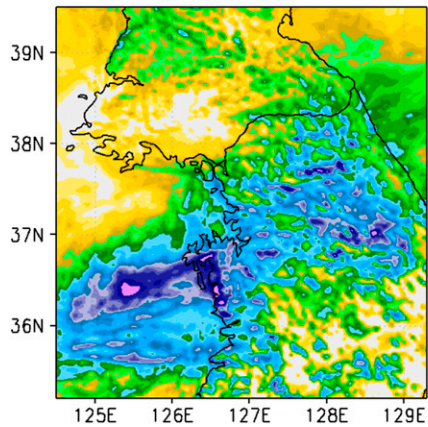
increasing tendency at higher resolutions. The steady or slight increase of CRR with grid size is not physically robust, because the role of CPS should decrease when the grid resolution becomes finer. It is also seen that the CRR stays in a similar range for the OSAS, GCIN, and GDTR runs. On the other hand, the CRR of GSAS shows a dramatic dependency on the horizontal grid resolution. While the contributions of CPS are over 90% at the 27- and 9-km resolutions, the CRR drops to 45% at the 3-km resolution and 10% at the 1-km resolution. The revised cloud-base mass flux (solid blue line) significantly reduces the CRR at higher resolutions (3 and 1 km), while it does not have a significant effect at 27- and 9-km resolutions. On the contrary, the modification made to GDTR (dotted blue line in Fig. 6) mainly influences the CRR at the lower resolutions (27 and 9 km) but not at the higher resolutions. This is because the detrainment of hydrometeors is suppressed at lower resolutions in the GSAS, whereas it is active irrespective of resolution in the case of OSAS. The sensitivity test of

individual modifications also confirms that the improvement of the precipitation forecast skill of the GSAS at 27- and 9-km resolutions is mostly due to the change made in convective cloud water detrainment (not shown). Unlike cloud-base mass flux and cloud water detrainment, the change in CIN (GCIN, dashed blue line) does not significantly affect CRR at all resolutions. Although the modification to CIN does not show a discernible impact, the removal of the CIN modification degrades the predictive skill, which suggests that the combined effects of CIN with the other two revisions are positive in the scale-aware CPS formulation.

The vertical distributions of the convective heating and drying rates in the OSAS and GSAS experiments are compared for all horizontal grid resolutions (Fig. 7). The maximum convective heating rate occurs at around 400 hPa, while the minimum drying rate occurs at 950 hPa in both the OSAS and GSAS results. This indicates that the updraft is reaching its maximum values

(a)  $(1 - \sigma_1)^2 \cdot CMF$ , total rainfall

(c) OSAS with GSAS BDY, total rainfall

(b)  $(1 - \sigma_2)^2 \cdot CMF$ , total rainfall

(d) GSAS with OSAS BDY, total rainfall

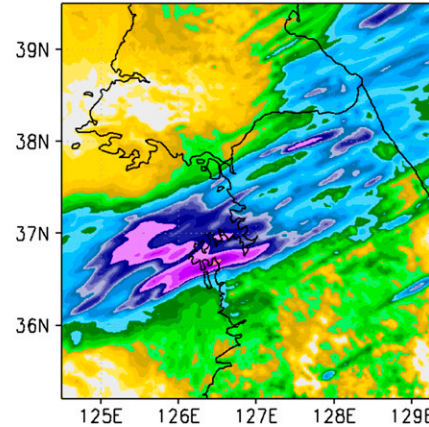


FIG. 8. The 24-h accumulated total rainfall of the sensitivity experiment results at  $dx = 3$  km. The cloud-base mass flux scaled by (a)  $(1 - \sigma_1)^2$  and (b)  $(1 - \sigma_2)^2$ ; the lateral boundary impacts are shown in (c) OSAS with the GSAS 9-km lateral BCs and (d) GSAS with the OSAS 9-km BCs.

in the upper troposphere and thus the transport of humid air from the PBL results in the saturation adjustment through the MPS processes. When the horizontal resolutions are increased from 27 to 1 km, the OSAS results do not show much variation in the magnitude of the heating and drying rates. Meanwhile, the heating and drying rates of the GSAS results decrease monotonically as the horizontal grid size decreases. This behavior of the GSAS runs confirms that the microphysics rain due to grid-scale saturation is more active at higher resolutions by suppressing convective activities, which is physically more sound and consistent with CRR, as shown in Fig. 6.

Another sensitivity test confirms that the cloud-base mass flux scaled by the combination of two sigmas ( $\sigma_1$  and  $\sigma_2$ ) produces much better results than that using an

individual sigma. The method of using  $(1 - \sigma_1)^2$  to modify the mass flux (Fig. 8a) produces rainfall patterns similar to those of the NOCP with significantly suppressed convection (Fig. 4c). On the other hand, the simulation results with the mass flux scaled by  $(1 - \sigma_2)^2$  show rainfall patterns similar to those of the OSAS (Fig. 4a) because of the insufficient resolution dependency of  $\sigma_2$ . More detailed studies intended to clarify the mechanisms of the positive interactions between two different cloud updraft fractions with more sets of sensitivity experiments are in progress.

An additional sensitivity experiment is performed to confirm that the improvements of the 3-km GSAS are derived from the modifications made in the convection scheme but not from the 9-km GSAS lateral boundary conditions (BCs). To examine the impact of the BCs, a

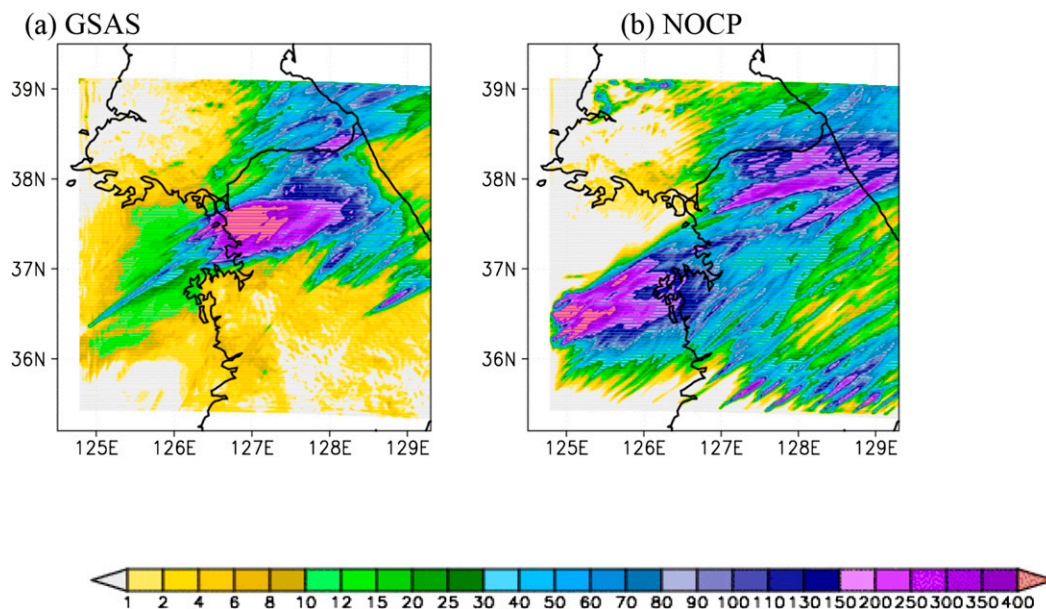


FIG. 9. The spatial distributions of 24-h accumulated total rainfall amount (mm) for 1200 UTC 27 Jul 2011 at 1-km resolution for (a) GSAS and (b) NOCP.

simulation of the 3-km OSAS with the 9-km GSAS boundary conditions (Fig. 8c) and a simulation of the 3-km GSAS with the 9-km OSAS boundary conditions (Fig. 8d) are conducted. The results indicate that swapping the BCs does not significantly impact the overall performance of the OSAS and GSAS. Therefore, the improvement seen in this study mostly comes from the modifications made in the CPS.

### c. 1-km resolution results

The general consensus is that it is better to run numerical models without calling a CPS at 1-km horizontal resolution, because most of the convection might be resolved at that resolution, and the use of a conventional CPS at this resolution is known to greatly degrade the model performance (Hong and Dudhia 2012). Even at a 1-km resolution, however, the newly developed GSAS shows its ability to reproduce the heavy rainfall core (Fig. 9a). The convective activity at 1-km resolution, despite the small amount ( $\sim 10\%$  according to Fig. 6), turns out to play a crucial role in organizing the precipitation band.

### d. One-month simulation results

July of 2011 produced not only greater amounts of precipitation over the Korean Peninsula but also had larger temporal variations in rainfall than for climatology (Moon et al. 2014). The model setup for this 1-month integration is the same as that for the heavy rainfall simulation described in section 2, with the initial

conditions at 0000 UTC 1 July 2011. To prevent the synoptic-scale drift, spectral nudging is employed. Thus, the large-scale information from the FNL data is nudged in the inner domains along with the lateral boundary conditions every 6 h. This kind of regional climate framework can be a useful test bed in evaluating the physics parameterization since the large-scale forcing is preserved during the model integration (Ghan et al. 1999). The 9-km output with the GSAS scheme is used to drive 3-km simulations with GSAS and NOCP runs. Shown in this section is the comparison of daily statistical skill scores between the two 3-km experiments for one month with 31 samples.

The observed precipitation pattern around the Korean Peninsula reveals the maximum rainfall amount is located across the middle of the peninsula with a secondary maximum along the southern coast (Figs. 10a,b). The results from both the NOCP and GSAS runs produce quite well matching precipitation patterns (Figs. 10c,d). These similarities might be partly due to the use of spectral nudging, which forces the simulation field to the analysis. Another reason for the relative success of the NOCP run in the 1-month simulation is due to the fact that the summer monsoonal precipitation over South Korea is driven by a synoptically strong environment rather than thermodynamically buoyant conditions (Hong 2004).

While the GSAS run underestimates the core rainfall amount as compared to the observations, the locations of the two maxima are well simulated. Although the



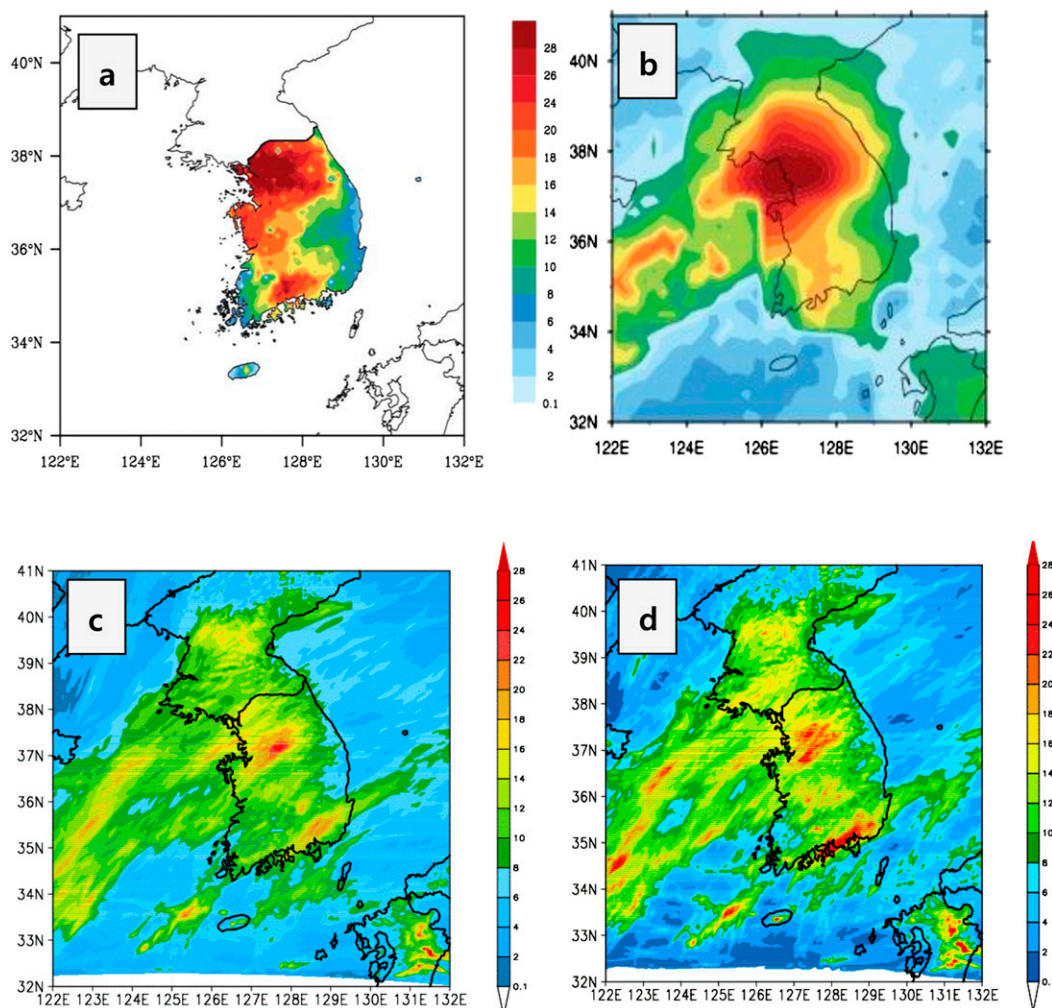


FIG. 10. The 1-month accumulated precipitation ( $\text{mm day}^{-1}$ ) during Jul 2011 obtained from (a) AWS and (b) TMPA. The 1-month simulated rainfall ( $\text{mm day}^{-1}$ ) from the 3-km-resolution WRF Model (c) with GSAS and (d) without CPS are also shown.

NOCP run also produces precipitation locations close to the observed cores, it produces some excessive rainfall amounts along the southern coast of South Korea, the Japanese island of Kyushu, and the Yellow Sea as compared to the observations and GSAS. Although it may be hard to discern in Fig. 10, the statistical skill of the simulated precipitation is comparable or slightly better when the GSAS is used. For example, the computed pattern correlation coefficients are 0.61 and 0.55 for the GSAS and NOCP runs, respectively. In addition to pattern correlation, the RMSE, equitable threat score (ETS), and false alarm ratio (FAR) also confirm that the GSAS results are superior to the NOCP outputs in most of the precipitation categories (Table 3). The time series of the hourly precipitation amount over South Korea in Fig. 11 demonstrate that the temporal evolution of precipitation is well simulated in

both the GSAS and NOCP runs with correlation coefficients of 0.72 and 0.73, respectively.

#### 4. Discussion and conclusions

The CPS gray-zone (1–10 km) problem has been a hot topic in the numerical weather modeling community recently because of increases in computing power. Regional modeling communities faced this problem in the early 2000s, and global models for NWP have started to reach the CPS gray-zone resolutions. The proper definition of the convective updraft fraction  $\sigma$  is the most crucial factor to consider when resolving the CPS gray-zone problem. In this study, the horizontal grid-size-dependent  $\sigma_1$  and the grid-scale updraft velocity-dependent  $\sigma_2$  are proposed as factors to modulate triggering condition, cloud water detrainment,

TABLE 3. Comparison of RMSE, PC, ETS, and FAR results from AWS observations for 1-month simulation from 1 to 31 Jul 2011. Better scores between NOCP and GSAS are highlighted in boldface.

Expt	RMSE	PC	Precipitation category (mm)	ETS	FAR
NOCP	31.59	0.55	<5	0.37	<b>0.28</b>
			10	0.36	0.29
			15	0.35	0.30
			20	0.33	0.31
			25	0.31	0.34
GSAS	<b>29.52</b>	<b>0.61</b>	<5	<b>0.38</b>	0.31
			10	<b>0.39</b>	<b>0.27</b>
			15	<b>0.38</b>	<b>0.24</b>
			20	<b>0.36</b>	<b>0.24</b>
			25	<b>0.32</b>	<b>0.28</b>

and cloud mass flux in a NCEP SAS CPS for gray-zone resolutions.

According to [Arakawa and Wu \(2013\)](#),  $(1 - \sigma)^2$  is the factor to use for modifying the convective fluxes in order to make a convection scheme valid across CPS gray-zone resolutions. Two convective updraft fractions are tested in this study: grid-size-dependent  $\sigma_1$  and grid-scale updraft-dependent  $\sigma_2$ . The tests conducted in this study suggest that the combination of two convective updraft fractions,  $(1 - \sigma_1)(1 - \sigma_2)$ , produces better results than using only one kind of  $\sigma$ , such as  $(1 - \sigma_1)^2$  or  $(1 - \sigma_2)^2$ . It is found from sensitivity tests that the combination of two updraft fractions complements each scheme's weaknesses (i.e., the lack of physical meaning of  $\sigma_1$  and the lack of magnitude variability of  $\sigma_2$  at different resolutions). The nonlinear interaction between the parameterized convection due to the CPS and grid-resolvable convection due to the MPS is assumed to be properly represented at a given resolution through the combined effects of two different convective updraft fractions. Both CIN and the amount of cloud water detrainment are modified to be functions of  $\sigma_1$ , so there is less convective trigger and more cloud water detrainment at higher resolutions.

To test the newly developed SAS CPS with scale-aware capability (GSAS), a series of experiments with the WRF Model was performed with four nested domains. The resolutions of the domains are set to 27, 9, 3, and 1 km to include the gray-zone CPS resolutions. A heavy rainfall case around the central part of the Korean Peninsula on 27 July 2011 is chosen for the experiments. The precipitation simulation results show that the GSAS performed significantly better than the original OSAS over all four domains in terms of precipitation patterns and maximum rainfall amount. With the GSAS, the typical gray-zone CPS problems on the 3- and 1-km grids are greatly alleviated with a well-organized single rainfall core, as in the observations, whereas the patterns of the simulated rainfall are widespread with weakened intensity in the case of the OSAS run. Intense but spurious multiple cores are generated when the CPS is removed. The results from sensitivity experiments indicate that the modifications to the cloud-base mass flux mostly influence the performance at higher resolutions. The modification of convective cloud water detrainment, on the other hand, mainly impacts the simulated precipitation at lower resolutions. The modified convective inhibition suppresses the subgrid convection at higher resolutions, but the results are not as significant as for the effects of the modified mass flux. The physical reasoning of scale-dependent triggering is rather weak, which can be elaborated upon further in the future. The 1-month simulation during July 2011 over the Korean Peninsula also shows comparable or slightly better precipitation prediction skills in GSAS than NOCP at 3-km resolution. Since the precipitation mechanism over South Korea in summer is largely governed by synoptically strong environments, the proportion of MPS rain to the total precipitation is relatively higher than for precipitation that is controlled by thermally driven conditions [see [Hong \(2004\)](#)]. The GSAS formulas could be elaborated upon by testing the results for

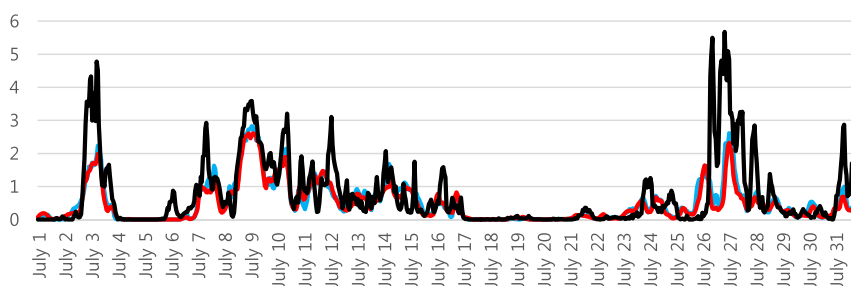


FIG. 11. The time series of the hourly rainfall observed by AWS over South Korea, the 3-km GSAS simulation, and the 3-km NOCP simulations are shown in black, red, and blue lines, respectively.

area of precipitating convection at geographically different areas around the globe.

**Acknowledgments.** This work was carried out through the research and development project on the development of global numerical weather prediction systems of the Korea Institute of Atmospheric Prediction Systems (KIAPS) funded by the Korea Meteorological Administration (KMA). The authors also want to express gratitude to Ms. Haneul Jeong for helping data analysis and proofreading.

## REFERENCES

- Arakawa, A., 2004: The cumulus parameterization problem: Past, present, and future. *J. Climate*, **17**, 2493–2525, doi:[10.1175/1520-0442\(2004\)017<2493:RATCPP>2.0.CO;2](https://doi.org/10.1175/1520-0442(2004)017<2493:RATCPP>2.0.CO;2).
- , and W. H. Schubert, 1974: Interaction of a cumulus cloud ensemble with the large-scale environment, Part I. *J. Atmos. Sci.*, **31**, 674–701, doi:[10.1175/1520-0469\(1974\)031<0674:IOACCE>2.0.CO;2](https://doi.org/10.1175/1520-0469(1974)031<0674:IOACCE>2.0.CO;2).
- , and C. M. Wu, 2013: A unified representation of deep moist convection in numerical modeling of the atmosphere. Part I. *J. Atmos. Sci.*, **70**, 1977–1992, doi:[10.1175/JAS-D-12-0330.1](https://doi.org/10.1175/JAS-D-12-0330.1).
- , J. H. Jung, and C. M. Wu, 2011: Toward unification of the multiscale modeling of the atmosphere. *Atmos. Chem. Phys.*, **11**, 3731–3742, doi:[10.5194/acp-11-3731-2011](https://doi.org/10.5194/acp-11-3731-2011).
- Bechtold, P., N. Semane, P. Lopez, J.-P. Charoureau, A. Beljaars, and N. Bormann, 2014: Representing equilibrium and non-equilibrium convection in large-scale models. *J. Atmos. Sci.*, **71**, 734–753, doi:[10.1175/JAS-D-13-0163.1](https://doi.org/10.1175/JAS-D-13-0163.1).
- Betts, A., and M. J. Miller, 1986: A new convective adjustment scheme. Part II: Single column tests using GATE wave, BOMEX and arctic air-mass data sets. *Quart. J. Roy. Meteor. Soc.*, **112**, 693–709, doi:[10.1002/qj.49711247308](https://doi.org/10.1002/qj.49711247308).
- Bryan, G. H., and H. Morrison, 2012: Sensitivity of a simulated squall line to horizontal resolution and parameterization of microphysics. *Mon. Wea. Rev.*, **140**, 202–225, doi:[10.1175/MWR-D-11-00046.1](https://doi.org/10.1175/MWR-D-11-00046.1).
- Chen, F., and J. Dudhia, 2001: Coupling an advanced land surface–hydrology model with the Penn State–NCAR MM5 modeling system. Part I: Model implementation and sensitivity. *Mon. Wea. Rev.*, **129**, 569–585, doi:[10.1175/1520-0493\(2001\)129<0569:CAALSH>2.0.CO;2](https://doi.org/10.1175/1520-0493(2001)129<0569:CAALSH>2.0.CO;2).
- Clark, A. J., J. S. Kain, P. T. Marsh, J. Correia, M. Xue, and F. Kong, 2012: Forecasting tornado pathlengths using a three-dimensional object identification algorithm applied to convection-allowing forecasts. *Wea. Forecasting*, **27**, 1090–1113, doi:[10.1175/WAF-D-11-00147.1](https://doi.org/10.1175/WAF-D-11-00147.1).
- Ek, M. B., K. E. Mitchell, Y. Lin, E. Rogers, P. Grunmann, V. Koren, G. Gayno, and J. D. Tarpley, 2003: Implementation of Noah land surface model advances in the National Centers for Environmental Prediction operational mesoscale eta model. *J. Geophys. Res.*, **108**, 8851, doi:[10.1029/2002JD003296](https://doi.org/10.1029/2002JD003296).
- Fowler, L. D., W. Skamarock, G. A. Grell, S. E. Freitas, and M. G. Duda, 2016: Analyzing the Grell–Freitas convection scheme from hydrostatic to nonhydrostatic scales within a global model. *Mon. Wea. Rev.*, **144**, 2285–2306, doi:[10.1175/MWR-D-15-0311.1](https://doi.org/10.1175/MWR-D-15-0311.1).
- Gerard, L., J. M. Piriou, R. Brožková, J. F. Geleyn, and D. Banciu, 2009: Cloud and precipitation parameterization in a meso-gamma-scale operational weather prediction model. *Mon. Wea. Rev.*, **137**, 3960–3977, doi:[10.1175/2009MWR2750.1](https://doi.org/10.1175/2009MWR2750.1).
- Ghan, S. J., L. R. Reung, and J. McCaa, 1999: A comparison of three different modeling strategies for evaluating cloud and radiation parameterizations. *Mon. Wea. Rev.*, **127**, 1967–1984, doi:[10.1175/1520-0493\(1999\)127<1967:ACOTDM>2.0.CO;2](https://doi.org/10.1175/1520-0493(1999)127<1967:ACOTDM>2.0.CO;2).
- Gomes, J. L., and S. C. Chou, 2010: Dependence of partitioning of model implicit and explicit precipitation on horizontal resolution. *Meteor. Atmos. Phys.*, **106**, 1–18, doi:[10.1007/s00703-009-0050-7](https://doi.org/10.1007/s00703-009-0050-7).
- Grell, G. A., 1993: Prognostic evaluation of assumptions used by cumulus parameterizations. *Mon. Wea. Rev.*, **121**, 764–787, doi:[10.1175/1520-0493\(1993\)121<0764:PEOAU>2.0.CO;2](https://doi.org/10.1175/1520-0493(1993)121<0764:PEOAU>2.0.CO;2).
- , and S. R. Freitas, 2014: A scale and aerosol aware stochastic convective parameterization for weather and air quality modeling. *Atmos. Chem. Phys.*, **14**, 5233–5250, doi:[10.5194/acp-14-5233-2014](https://doi.org/10.5194/acp-14-5233-2014).
- Han, J., and H. L. Pan, 2011: Revision of convection and vertical diffusion schemes in the NCEP Global Forecast System. *Wea. Forecasting*, **26**, 520–533, doi:[10.1175/WAF-D-10-05038.1](https://doi.org/10.1175/WAF-D-10-05038.1).
- Hong, S.-Y., 2004: Comparison of heavy rainfall mechanisms in Korea and the central US. *J. Meteor. Soc. Japan*, **82**, 1469–1479, doi:[10.2151/jmsj.2004.1469](https://doi.org/10.2151/jmsj.2004.1469).
- , and H.-L. Pan, 1998: Convective trigger function for a mass flux cumulus parameterization scheme. *Mon. Wea. Rev.*, **126**, 2599–2620, doi:[10.1175/1520-0493\(1998\)126<2599:CTFFAM>2.0.CO;2](https://doi.org/10.1175/1520-0493(1998)126<2599:CTFFAM>2.0.CO;2).
- , and J. Dudhia, 2012: Next-generation numerical weather prediction: Bridging parameterization, explicit clouds, and large eddies. *Bull. Amer. Meteor. Soc.*, **93**, ES6–ES9, doi:[10.1175/2011BAMS3224.1](https://doi.org/10.1175/2011BAMS3224.1).
- , —, and S.-H. Chen, 2004: A revised approach to ice microphysical processes for the bulk parameterization of clouds and precipitation. *Mon. Wea. Rev.*, **132**, 103–120, doi:[10.1175/1520-0493\(2004\)132<0103:ARATIM>2.0.CO;2](https://doi.org/10.1175/1520-0493(2004)132<0103:ARATIM>2.0.CO;2).
- , Y. Noh, and J. Dudhia, 2006: A new vertical diffusion package with an explicit treatment of entrainment processes. *Mon. Wea. Rev.*, **134**, 2318–2341, doi:[10.1175/MWR3199.1](https://doi.org/10.1175/MWR3199.1).
- , J. Jang, J. Lee, J. Dudhia, and W. Wang, 2013: The GRIMs shallow convection scheme. *Proc. 14th Annual WRF User's Workshop*, Boulder, CO, NCAR. [Available online at <http://www2.mmm.ucar.edu/wrf/users/workshops/WS2013/posters/p97.pdf>.]
- Iacono, M. J., J. S. Delamere, E. J. Mlawer, M. W. Shephard, S. A. Clough, and W. D. Collins, 2008: Radiative forcing by long-lived greenhouse gases: Calculations with the AER radiative transfer models. *J. Geophys. Res.*, **113**, D13103, doi:[10.1029/2008JD009944](https://doi.org/10.1029/2008JD009944).
- Jang, J., and S.-Y. Hong, 2014: Quantitative forecast experiment of a heavy rainfall event over Korea in a global model: Horizontal resolution versus lead time issues. *Meteor. Atmos. Phys.*, **124**, 113–127, doi:[10.1007/s00703-014-0312-x](https://doi.org/10.1007/s00703-014-0312-x).
- Kain, J. S., 2004: The Kain–Fritsch convective parameterization: An update. *J. Appl. Meteor.*, **43**, 170–181, doi:[10.1175/1520-0450\(2004\)043<0170:TKCPAU>2.0.CO;2](https://doi.org/10.1175/1520-0450(2004)043<0170:TKCPAU>2.0.CO;2).
- , and J. M. Fritsch, 1990: A one-dimensional entraining/detraining plume model and its application in convective parameterization. *J. Atmos. Sci.*, **47**, 2784–2802, doi:[10.1175/1520-0469\(1990\)047<2784:AODEPM>2.0.CO;2](https://doi.org/10.1175/1520-0469(1990)047<2784:AODEPM>2.0.CO;2).
- Koo, M.-S., S.-Y. Hong, and J. Kim, 2009: An evaluation of the Tropical Rainfall Measuring Mission (TRMM) Multi-Satellite Precipitation Analysis (TMPA) data over South Korea. *Asia-Pac. J. Atmos. Sci.*, **45**, 265–282.
- Kuettl, V., A. Gassmann, and A. Bott, 2007: Towards a new hybrid cumulus parametrization scheme for use in non-hydrostatic weather prediction models. *Quart. J. Roy. Meteor. Soc.*, **133**, 479–490, doi:[10.1002/qj.28](https://doi.org/10.1002/qj.28).
- Kuo, H. L., 1974: Further studies of the parameterization of the influence of cumulus convection on large-scale flow. *J. Atmos.*

- Sci.*, **31**, 1232–1240, doi:[10.1175/1520-0469\(1974\)031<1232:FSOTPO>2.0.CO;2](https://doi.org/10.1175/1520-0469(1974)031<1232:FSOTPO>2.0.CO;2).
- Lim, K.-S. S., S.-Y. Hong, J.-H. Yoon, and J. Han, 2014: Simulation of the summer monsoon rainfall over East Asia using the NCEP GFS cumulus parameterization at different horizontal resolutions. *Wea. Forecasting*, **29**, 1143–1154, doi:[10.1175/WAF-D-13-00143.1](https://doi.org/10.1175/WAF-D-13-00143.1).
- McMillen, J. D., and W. J. Steenburgh, 2015: Impact of microphysics parameterizations on simulations of the 27 October 2010 Great Salt Lake–effect snowstorm. *Wea. Forecasting*, **30**, 136–152, doi:[10.1175/WAF-D-14-00060.1](https://doi.org/10.1175/WAF-D-14-00060.1).
- Mlawer, E. J., S. J. Taubman, P. D. Brown, M. J. Iacono, and S. A. Clough, 1997: Radiative transfer for inhomogeneous atmospheres: RRTM, a validated correlated-k model for the longwave. *J. Geophys. Res.*, **102**, 16 663–16 682, doi:[10.1029/97JD00237](https://doi.org/10.1029/97JD00237).
- Moon, J.-Y., Y.-A. Kwon, Y.-E. Choi, and I.-H. Park, 2014: A study on the characteristics of summer rainfall over South Korea in recent 5 years. *Climate Res.*, **9**, 269–282, doi:[10.14383/cr.2014.9.4.269](https://doi.org/10.14383/cr.2014.9.4.269).
- Pan, H.-L., and W.-S. Wu, 1995: Implementing a mass flux convective parameterization package for the NMC Medium Range Forecast model. NMC Office Note 409, 40 pp. [Available online at [http://www2.mmm.ucar.edu/wrf/users/phys\\_refs/CU\\_PHYS/Old\\_SAS.pdf](http://www2.mmm.ucar.edu/wrf/users/phys_refs/CU_PHYS/Old_SAS.pdf).]
- , Q. Liu, J. Han, and R. Sun, 2014: Extending the simplified Arakawa-Schubert scheme for meso-scale model applications. NCEP Office Note 479, 10 pp. [Available online at <http://www.lib.ncep.noaa.gov/ncepooffice/notes/files/on479.pdf>.]
- Qiao, F., and X. Z. Liang, 2014: Effects of cumulus parameterizations on predictions of summer flood in the central United States. *Climate Dyn.*, **45**, 727–744, doi:[10.1007/s00382-014-2301-7](https://doi.org/10.1007/s00382-014-2301-7).
- Schwartz, C. S., and Z. Liu, 2014: Convection-permitting forecasts initialized with continuously cycling limited-area 3DVAR, ensemble Kalman filter, and “hybrid” variational–ensemble data assimilation systems. *Mon. Wea. Rev.*, **142**, 716–738, doi:[10.1175/MWR-D-13-00100.1](https://doi.org/10.1175/MWR-D-13-00100.1).
- Skamarock, W. C., and Coauthors, 2008: A description of the Advanced Research WRF version 3. NCAR Tech. Note NCAR/TN-475+STR, 113 pp., doi:[10.5065/D68S4MVH](https://doi.org/10.5065/D68S4MVH).
- Tiedtke, M., 1989: A comprehensive mass flux scheme for cumulus parameterization in large-scale models. *Mon. Wea. Rev.*, **117**, 1779–1800, doi:[10.1175/1520-0493\(1989\)117<1779:ACMFSF>2.0.CO;2](https://doi.org/10.1175/1520-0493(1989)117<1779:ACMFSF>2.0.CO;2).
- Wang, Y.-C., H.-L. Pan, and H.-H. Hsu, 2015: Impacts of the triggering function of cumulus parameterization on warm-season diurnal rainfall cycles at the atmospheric radiation measurement Southern Great Plains site. *J. Geophys. Res. Atmos.*, **120**, 10 681–10 702, doi:[10.1002/2015JD023337](https://doi.org/10.1002/2015JD023337).
- Zhang, G. J., and N. A. McFarlane, 1995: Sensitivity of climate simulations to the parameterization of cumulus convection in the Canadian Climate Centre general circulation model. *Atmos.–Ocean*, **33**, 407–446, doi:[10.1080/07055900.1995.9649539](https://doi.org/10.1080/07055900.1995.9649539).
- Zhao, Q., and F. H. Carr, 1997: A prognostic cloud scheme for operational NWP models. *Mon. Wea. Rev.*, **125**, 1931–1953, doi:[10.1175/1520-0493\(1997\)125<1931:APCSFO>2.0.CO;2](https://doi.org/10.1175/1520-0493(1997)125<1931:APCSFO>2.0.CO;2).
- Zheng, Y., K. Alapaty, J. A. Herwehe, A. D. Del Genio, and D. Niyogi, 2016: Improving high-resolution weather forecasts using the Weather Research and Forecasting (WRF) Model with an updated Kain–Fritsch scheme. *Mon. Wea. Rev.*, **144**, 833–860, doi:[10.1175/MWR-D-15-0005.1](https://doi.org/10.1175/MWR-D-15-0005.1).